Laser-induced torques in metallic antiferromagnets

Frank Freimuth,[1,2,*] Stefan Blügel,[1] and Yuriy Mokrousov[1,2]
[1]*Peter Grünberg Institut and Institute for Advanced Simulation, Forschungszentrum Jülich and JARA, 52425 Jülich, Germany*
[2]*Institute of Physics, Johannes Gutenberg University Mainz, 55099 Mainz, Germany*

(Received 29 March 2021; revised 10 May 2021; accepted 10 May 2021; published 24 May 2021)

We study laser-induced torques in the antiferromagnet Mn_2Au. We find that even linearly polarized light may induce laser-induced torques in Mn_2Au; that is, the light does not have to be circularly polarized. The laser-induced torques in Mn_2Au are comparable in magnitude to those in the ferromagnets Fe, Co, and FePt at optical frequencies. We also compute the laser-induced torques at terahertz (THz) frequencies and compare them to the spin-orbit torques (SOTs) excited by THz laser pulses. We find the SOTs are dominant at THz frequencies for the laser-field strengths used in experiments. Additionally, we show that the matrix elements of the spin-orbit interaction (SOI) can be used to add SOI only during the Wannier interpolation, which we call Wannier interpolation of SOI. This technique allows us to perform the Wannier interpolation conveniently for many magnetization directions from a single set of Wannier functions.

DOI: 10.1103/PhysRevB.103.174429

I. INTRODUCTION

Using femtosecond laser pulses to switch the magnetization [1,2], to exert torques on the magnetic moments [3–11], to move domain walls [12], and to excite magnons [13] is a promising concept to write, store, and process information on ultrafast timescales in prospective device applications. In bulk crystals laser-induced torques on the magnetization are attributed to the inverse Faraday effect (IFE) and to the optical spin-transfer torque (OSTT) [3,4,11]. Phenomenology for nonmagnets predicts the IFE only for circularly polarized light. However, works on the ferromagnetic Rashba model [14] as well as first-principles calculations [11,15] show that the IFE in ferromagnets differs from these predictions; that is, the IFE is present even for linearly polarized light.

Due to their terahertz (THz) magnetization dynamics, antiferromagnets (AFMs) are another promising ingredient in ultrafast magnetism concepts [16–19]. To this end, spin-orbit torques (SOTs) in the bulk AFM Mn_2Au have been studied intensively both in theory [20–22] and in experiment [23–26], and it has been shown that the SOT may be used to switch the Néel vector. For the optical manipulation of the Néel vector the IFE and OSTT might be promising alternatives to the SOT. However, theoretical works on the IFE and OSTT in AFMs are still lacking.

When lasers at optical frequencies are used to exert torques in AFMs, it is clear that the SOT excited by the electric field of the laser may be ignored because it is oscillating at the laser frequency, which is far above the magnetic resonances in the AFMs in the THz range. This picture changes when THz lasers are used to excite the magnetization in AFMs. In Ref. [19] THz laser pulses were used to switch the AFM CuMnAs contactlessly, and this switching was interpreted as the action of the SOT. While the SOT is linear in the applied electric field, the IFE and OSTT are quadratic in it. The question therefore is at which electric field strength the IFE and OSTT become more important than the SOT when the frequency of the applied electric field is in the THz range.

In this work we investigate the laser-induced torques in the bulk AFM Mn_2Au. Our computational approach is based on the Keldysh nonequilibrium formalism and on the Wannier interpolation [27] of the electronic structure obtained from realistic density-functional theory calculations. In order to study the dependence of the laser-induced torques on the magnetization direction we introduce a method that allows us to do the Wannier interpolation conveniently for many different magnetization directions on the basis of a single set of maximally localized Wannier functions (MLWFs), which we call Wannier interpolation of spin-orbit interaction (WISOI).

This paper is organized as follows. In Sec. II A we briefly review the formalism that we use to compute the laser-induced torque. In Sec. II B we describe WISOI briefly, deferring details on the implementation to the Appendix. In Sec. II C we discuss how the symmetry of the Mn_2Au crystal determines the form of the response tensor. In Sec. III we discuss our results for the laser-induced torques in Mn_2Au. This paper ends with a summary in Sec. IV.

II. FORMALISM

A. Keldysh formalism

In Ref. [11] we derived the following expression for the laser-induced torque based on the Keldysh nonequilibrium formalism:

$$T_i = \frac{a_0^3 I}{c}\left(\frac{\mathcal{E}_\mathrm{H}}{\hbar\omega}\right)^2 \mathrm{Im}\sum_{jk}\epsilon_j\epsilon_k^*\chi_{ijk}, \tag{1}$$

*Corresponding author: f.freimuth@fz-juelich.de

where c is the velocity of light, $a_0 = 4\pi\epsilon_0\hbar^2/(me^2)$ is Bohr's radius, $I = \epsilon_0 c E_0^2/2$ is the intensity of light, ϵ_0 is the vacuum permittivity, $\mathcal{E}_\mathrm{H} = e^2/(4\pi\epsilon_0 a_0)$ is the Hartree energy, and ϵ_j is the jth Cartesian component of the light polarization vector. The tensor χ_{ijk} is given by

$$\begin{aligned}\chi_{ijk} = \frac{2}{\mathcal{N}\hbar a_0^2 \mathcal{E}_\mathrm{H}} \sum_{\boldsymbol{k}} \int d\mathcal{E} \mathrm{Tr}\big[& f(\mathcal{E}) \mathcal{T}_i G^\mathrm{R}_{\boldsymbol{k}}(\mathcal{E}) v_j G^\mathrm{R}_{\boldsymbol{k}}(\mathcal{E}-\hbar\omega) v_k G^\mathrm{R}_{\boldsymbol{k}}(\mathcal{E}) - f(\mathcal{E}) \mathcal{T}_i G^\mathrm{R}_{\boldsymbol{k}}(\mathcal{E}) v_j G^\mathrm{R}_{\boldsymbol{k}}(\mathcal{E}-\hbar\omega) v_k G^\mathrm{A}_{\boldsymbol{k}}(\mathcal{E}) \\ & + f(\mathcal{E}) \mathcal{T}_i G^\mathrm{R}_{\boldsymbol{k}}(\mathcal{E}) v_k G^\mathrm{R}_{\boldsymbol{k}}(\mathcal{E}+\hbar\omega) v_j G^\mathrm{R}_{\boldsymbol{k}}(\mathcal{E}) - f(\mathcal{E}) \mathcal{T}_i G^\mathrm{R}_{\boldsymbol{k}}(\mathcal{E}) v_k G^\mathrm{R}_{\boldsymbol{k}}(\mathcal{E}+\hbar\omega) v_j G^\mathrm{A}_{\boldsymbol{k}}(\mathcal{E}) \\ & + f(\mathcal{E}-\hbar\omega) \mathcal{T}_i G^\mathrm{R}_{\boldsymbol{k}}(\mathcal{E}) v_j G^\mathrm{R}_{\boldsymbol{k}}(\mathcal{E}-\hbar\omega) v_k G^\mathrm{A}_{\boldsymbol{k}}(\mathcal{E}) + f(\mathcal{E}+\hbar\omega) \mathcal{T}_i G^\mathrm{R}_{\boldsymbol{k}}(\mathcal{E}) v_k G^\mathrm{R}_{\boldsymbol{k}}(\mathcal{E}+\hbar\omega) v_j G^\mathrm{A}_{\boldsymbol{k}}(\mathcal{E}) \big], \end{aligned} \tag{2}$$

where $\mathcal{N}$ is the number of $\boldsymbol{k}$ points, $f(\mathcal{E})$ is the Fermi distribution function, $\boldsymbol{\mathcal{T}}$ is the torque operator, $\boldsymbol{v}$ is the velocity operator,

$$G^\mathrm{R}_{\boldsymbol{k}}(\mathcal{E}) = \hbar \sum_n \frac{|\boldsymbol{k}n\rangle\langle\boldsymbol{k}n|}{\mathcal{E} - \mathcal{E}_{\boldsymbol{k}n} + i\Gamma} \tag{3}$$

is the retarded Green's function, and $G^\mathrm{A}_{\boldsymbol{k}}(\mathcal{E}) = [G^\mathrm{R}_{\boldsymbol{k}}(\mathcal{E})]^\dagger$ is the advanced Green's function. Here, $|\boldsymbol{k}n\rangle$ and $\mathcal{E}_{\boldsymbol{k}n}$ are eigenstates and eigenenergies, respectively, and Γ is a constant broadening used to simulate disorder and finite lifetimes of the electronic states.

Our Green's function expressions provide an alternative approach to the expressions based on the order formalism [15,28] used to compute the IFE. In Ref. [29] we showed that Eq. (2) may be modified in order to compute laser-induced charge and spin photocurrents. Thus, the Keldysh formalism underlying Eq. (2) provides also an alternative approach to the method based on the expressions given first by von Baltz and Kraut [30–32].

In the case of the SOT one may distinguish spin and orbital torques [22,33–37]. For example, in TmIG/Pt/CuO_x the SOT has been interpreted in terms of an orbital current generated at the Pt/CuO_x interface, which is converted subsequently into a spin current by the SOI of Pt [34], and in Ni/W(110) calculations show that the SOT even differs in sign from the spin-transfer torque associated with the spin current of W [33] because the orbital torque dominates. However, when one computes the linear response of the torque operator $\boldsymbol{\mathcal{T}}$ to the applied electric field, one captures both the spin torque and the orbital torque. Therefore, in order to describe the SOT when the orbital torque dominates, one does not need a new formalism to compute the total SOT, but one might wish to develop additional tools to separate the total SOT into spin and orbital contributions [33].

In the case of the laser-induced torques it might become useful as well to distinguish between spin and orbital contributions. A strong indication that this might be the case is the finding of a large laser-induced orbital magnetization [15] even without SOI. However, the only mechanism by which this orbital magnetization may directly lead to a torque on the magnetization is through the Oersted field generated by the orbital photocurrent. Therefore, one may expect that a significantly larger torque arises from the coupling of the laser-induced orbital magnetization to the spin magnetization due to SOI. Such an indirect contribution from the laser-induced orbital magnetization to the laser-induced torque is already contained in the response of the torque operator $\boldsymbol{\mathcal{T}}$ to the applied laser field, and an extension of our formalism is not necessary. However, like in the case of the SOT, it might become desirable in the future to develop tools to separate the laser-induced torque into spin and orbital contributions. We leave the development of such tools for future work.

B. Wannier interpolation of SOI

In the presence of SOI the electronic structure depends on the direction of the (staggered) magnetization. When one would like to evaluate Eq. (2) for many different magnetization directions, one first needs to perform density-functional theory calculations of the electronic structure for all of them. If one uses Wannier interpolation for computational speedup of Eq. (2), one additionally needs to compute MLWFs for all these magnetization directions. Alternatively, one may compute the electronic structure and MLWFs without SOI and add the effect of SOI during the Wannier interpolation of the material property tensors. This is a very convenient approach when the material property tensors need to be evaluated for many magnetization directions.

We briefly explain this Wannier interpolation of SOI here and refer the reader to the Appendix for the details of our implementation of this approach. We denote the MLWFs without SOI by $|\bar{W}_{\boldsymbol{R}n\sigma}\rangle$, where $\sigma = \uparrow, \downarrow$ labels the spin. The number of spin-up MLWFs is $N_\uparrow$, and the number of spin-down MLWFs is $N_\downarrow$. The total number of MLWFs is $N_\mathrm{W} = N_\uparrow + N_\downarrow$. Using these MLWFs, we compute the matrix elements of the Hamiltonian $\bar{H}$ without SOI,

$$\bar{h}^{\sigma\sigma}_{\boldsymbol{R}nm} = \langle \bar{W}_{\boldsymbol{0}n\sigma} | \bar{H} | \bar{W}_{\boldsymbol{R}m\sigma} \rangle, \tag{4}$$

and, additionally, the following matrix elements:

$$\mathcal{A}^{\sigma\sigma' j}_{\boldsymbol{R}nm} = \sum_\alpha \langle \bar{W}_{\boldsymbol{0}n\sigma} | \xi_\alpha(\boldsymbol{r} - \boldsymbol{r}_\alpha) L^\alpha_j | \bar{W}_{\boldsymbol{R}m\sigma'} \rangle, \tag{5}$$

where L^α_j is the orbital angular momentum operator of atom α and $\xi_\alpha(\boldsymbol{r} - \boldsymbol{r}_\alpha)$ is the SOI potential in a sphere around atom α with its center at $\boldsymbol{r}_\alpha$. The index j takes the values z, $-$, and $+$, where $L^\alpha_+ = (L^\alpha_x + iL^\alpha_y)$ and $L^\alpha_- = (L^\alpha_x - iL^\alpha_y)$.

One needs to add $\mathcal{V}_\mathrm{SOI} = \sum_\alpha \xi_\alpha(\boldsymbol{r} - \boldsymbol{r}_\alpha) \boldsymbol{L}^\alpha \cdot \boldsymbol{\sigma}$ to $\bar{H}$ in order to include SOI in the calculation. To obtain the matrix elements $\mathcal{V}^{\sigma\sigma'}_{\boldsymbol{R}nm} = \langle \bar{W}_{\boldsymbol{0}n\sigma} | \mathcal{V}_\mathrm{SOI} | \bar{W}_{\boldsymbol{R}m\sigma'} \rangle$ when the Néel vector points in the direction $\hat{\boldsymbol{\mathcal{L}}} = (\sin\theta\cos\phi, \sin\theta\sin\phi, \cos\theta)^\mathrm{T}$, we need to multiply Eq. (5) with trigonometric functions of

the angles θ and ϕ as follows:

$$\boldsymbol{\mathcal{V}}_{\boldsymbol{R}}^{\uparrow\uparrow} = \boldsymbol{\mathcal{A}}_{\boldsymbol{R}}^{\uparrow\uparrow z}\cos\theta + \frac{1}{2}\boldsymbol{\mathcal{A}}_{\boldsymbol{R}}^{\uparrow\uparrow -}\sin\theta e^{i\phi} + \frac{1}{2}\boldsymbol{\mathcal{A}}_{\boldsymbol{R}}^{\uparrow\uparrow +}\sin\theta e^{-i\phi}, \tag{6}$$

$$\boldsymbol{\mathcal{V}}_{\boldsymbol{R}}^{\downarrow\downarrow} = -\boldsymbol{\mathcal{A}}_{\boldsymbol{R}}^{\downarrow\downarrow z}\cos\theta - \frac{1}{2}\boldsymbol{\mathcal{A}}_{\boldsymbol{R}}^{\downarrow\downarrow -}\sin\theta e^{i\phi} - \frac{1}{2}\boldsymbol{\mathcal{A}}_{\boldsymbol{R}}^{\downarrow\downarrow +}\sin\theta e^{-i\phi}, \tag{7}$$

$$\boldsymbol{\mathcal{V}}_{\boldsymbol{R}}^{\uparrow\downarrow} = -\boldsymbol{\mathcal{A}}_{\boldsymbol{R}}^{\uparrow\downarrow z}\sin\theta + \boldsymbol{\mathcal{A}}_{\boldsymbol{R}}^{\uparrow\downarrow -}\left[\cos\frac{\theta}{2}\right]^2 e^{i\phi} - \boldsymbol{\mathcal{A}}_{\boldsymbol{R}}^{\uparrow\downarrow +}\left[\sin\frac{\theta}{2}\right]^2 e^{-i\phi}, \tag{8}$$

and

$$\boldsymbol{\mathcal{V}}_{\boldsymbol{R}}^{\downarrow\uparrow} = -\boldsymbol{\mathcal{A}}_{\boldsymbol{R}}^{\downarrow\uparrow z}\sin\theta - \boldsymbol{\mathcal{A}}_{\boldsymbol{R}}^{\downarrow\uparrow -}\left[\sin\frac{\theta}{2}\right]^2 e^{i\phi} + \boldsymbol{\mathcal{A}}_{\boldsymbol{R}}^{\downarrow\uparrow +}\left[\cos\frac{\theta}{2}\right]^2 e^{-i\phi}. \tag{9}$$

Finally, the Wannier-interpolated Hamiltonian matrix including SOI is given by

$$H_{\boldsymbol{k}}^{\mathrm{W}} = \begin{pmatrix} \bar{\boldsymbol{h}}_{\boldsymbol{k}}^{\uparrow\uparrow} & 0 \\ 0 & \bar{\boldsymbol{h}}_{\boldsymbol{k}}^{\downarrow\downarrow} \end{pmatrix} + \begin{pmatrix} \boldsymbol{\mathcal{V}}_{\boldsymbol{k}}^{\uparrow\uparrow} & \boldsymbol{\mathcal{V}}_{\boldsymbol{k}}^{\uparrow\downarrow} \\ \boldsymbol{\mathcal{V}}_{\boldsymbol{k}}^{\downarrow\uparrow} & \boldsymbol{\mathcal{V}}_{\boldsymbol{k}}^{\downarrow\downarrow} \end{pmatrix}, \tag{10}$$

where the $N_\sigma \times N_{\sigma'}$ matrices $\bar{\boldsymbol{h}}_{\boldsymbol{k}}^{\sigma\sigma'}$ and $\boldsymbol{\mathcal{V}}_{\boldsymbol{k}}^{\sigma\sigma'}$ are the following Fourier transforms:

$$\bar{\boldsymbol{h}}_{\boldsymbol{k}}^{\sigma\sigma'} = \sum_{\boldsymbol{R}} e^{i\boldsymbol{k}\cdot\boldsymbol{R}}\bar{\boldsymbol{h}}_{\boldsymbol{R}}^{\sigma\sigma'}, \quad \boldsymbol{\mathcal{V}}_{\boldsymbol{k}}^{\sigma\sigma'} = \sum_{\boldsymbol{R}} e^{i\boldsymbol{k}\cdot\boldsymbol{R}}\boldsymbol{\mathcal{V}}_{\boldsymbol{R}}^{\sigma\sigma'}. \tag{11}$$

With this Wannier-interpolated Hamiltonian $H_{\boldsymbol{k}}^{\mathrm{W}}$ we proceed in the usual way; that is, it is diagonalized, and the eigenvalues and eigenvectors are used to evaluate Eq. (2). The velocity operator is obtained from $H_{\boldsymbol{k}}^{\mathrm{W}}$ as usual [27]:

$$\boldsymbol{v}_{\boldsymbol{k}} = \frac{1}{\hbar}\frac{\partial H_{\boldsymbol{k}}^{\mathrm{W}}}{\partial \boldsymbol{k}}. \tag{12}$$

C. Symmetry

In this section we discuss which components of the tensor χ_{ijk}, Eq. (2), are allowed by symmetry in the Mn_2Au crystal. For this purpose we expand the laser-induced torque in orders of the staggered magnetization $\mathcal{L}$ as follows:

$$T_i = \chi_{ijkl}^{(4\mathrm{sp})}E_jE_k^*\mathcal{L}_l + \chi_{ijklm}^{(5\mathrm{a})}E_jE_k^*\mathcal{L}_l\mathcal{L}_m + \cdots, \tag{13}$$

which implies that χ_{ijk} has the expansion

$$\chi_{ijk} = \chi_{ijkl}^{(4\mathrm{sp})}\mathcal{L}_l + \chi_{ijklm}^{(5\mathrm{a})}\mathcal{L}_l\mathcal{L}_m + \cdots. \tag{14}$$

First, we need to find out how the tensors $\chi_{ijkl}^{(4\mathrm{sp})}$ and $\chi_{ijklm}^{(5\mathrm{a})}$ transform under symmetry operations. We recall that polar tensors satisfy

$$\chi_{i'j'k'l'\ldots}^{\mathrm{p}} = \chi_{ijkl\ldots}^{\mathrm{p}}\mathcal{R}_{ii'}\mathcal{R}_{jj'}\mathcal{R}_{kk'}\mathcal{R}_{ll'}\cdots \tag{15}$$

for all symmetry operations $\mathcal{R}$ in the point group of the space group of the crystal, while axial tensors satisfy

$$\chi_{i'j'k'l'\ldots}^{\mathrm{a}} = (-1)^{\det\mathcal{R}}\chi_{ijkl\ldots}^{\mathrm{a}}\mathcal{R}_{ii'}\mathcal{R}_{jj'}\mathcal{R}_{kk'}\mathcal{R}_{ll'}\cdots. \tag{16}$$

In general, a staggered field, i.e., a field that switches sign between different magnetic sublattices, transforms differently from a nonstaggered field. For this reason the introduction of polar and axial response tensors is insufficient to describe all possible responses in antiferromagnets. Therefore, we need to introduce two more types of tensors, namely, staggered polar and staggered axial tensors. In antiferromagnets with two magnetic sublattices that are not related by a lattice translation these two additional types of tensors may be defined as follows: We call a tensor *staggered polar* when it satisfies

$$\chi_{i'j'k'l'\ldots}^{\mathrm{sp}} = (-1)^{S(\mathcal{R})}\chi_{ijkl\ldots}^{\mathrm{sp}}\mathcal{R}_{ii'}\mathcal{R}_{jj'}\mathcal{R}_{kk'}\mathcal{R}_{ll'}\cdots \tag{17}$$

for all $\mathcal{R}$ in the point group. Here, $S(\mathcal{R}) = -1$ if $\mathcal{R}$ interchanges the two sublattices, and $S(\mathcal{R}) = 1$ otherwise. Similarly, we call a tensor *staggered axial* when it satisfies

$$\chi_{i'j'k'l'\ldots}^{\mathrm{sa}} = (-1)^{S(\mathcal{R})}(-1)^{\det\mathcal{R}}\chi_{ijkl\ldots}^{\mathrm{sa}}\mathcal{R}_{ii'}\mathcal{R}_{jj'}\mathcal{R}_{kk'}\mathcal{R}_{ll'}\cdots \tag{18}$$

for all $\mathcal{R}$ in the point group.

The Néel vector $\mathcal{L}$ transforms like a staggered axial tensor of rank 1. Consequently, $\chi_{ijkl}^{(4\mathrm{sp})}$ is a staggered polar tensor of rank 4, and $\chi_{ijklm}^{(5\mathrm{a})}$ is an axial tensor of rank 5. Our expansion in Eq. (13) has the advantage that it can be applied for a general direction of $\boldsymbol{\mathcal{L}}$ and that only information on the point group and on the positions of the magnetic sublattice sites is required to determine the tensors allowed by symmetry. In contrast, the usual symmetry analysis based on the magnetic point groups suffers from the fact that in the presence of SOI the magnetic point group depends on the direction of $\boldsymbol{\mathcal{L}}$. Determining the response tensors allowed by the magnetic point groups for selected high-symmetry directions of $\boldsymbol{\mathcal{L}}$ provides less information than our expansion (13).

Next, we need to find out which components of the tensors are consistent with all symmetry operations $\mathcal{R}$. We find that in Mn_2Au staggered polar tensors of rank 4 are not allowed by symmetry. However, axial tensors of rank 5 are allowed, and we find 30 such tensors. In order to discuss these tensors we introduce the notation

$$\delta_{nopqr}^{(ijklm)} = \delta_{in}\delta_{jo}\delta_{kp}\delta_{lq}\delta_{mr} \rightarrow \langle ijklm\rangle. \tag{19}$$

The 30 axial tensors of rank 5 allowed by symmetry in Mn_2Au are listed in Table I.

Since only torques that are perpendicular to the Néel vector are relevant, we do not need to consider tensor components, where the first index is equal to the last two indices. Therefore, we may ignore tensors 1, 16, and 28 (indicated by $\emptyset$ in Table I). Additionally, we may ignore tensor 25 because the indices l and m are interchangeable in the second term on the right-hand side of Eq. (14). The number of tensors that need to be considered may be reduced further by noting that indices l and m in $\chi_{ijklm}^{(5\mathrm{a})}$ are both contracted with the staggered magnetization, while indices j and k are both contracted with the electric field. Therefore, when the tensors in Table I are inserted into Eq. (14), several of them are effectively equivalent. If a tensor does not need to be considered due to this equivalency it is denoted by $\{r\}$ in Table I, where r is the tensor that can be used to replace this tensor.

In Mn_2Au the Néel vector $\boldsymbol{\mathcal{L}}$ lies in the xy plane. Therefore, we first discuss possible tensors $\chi_{ijklm}^{(5\mathrm{a})}$ where indices 4 and 5 take values corresponding to in-plane $\boldsymbol{\mathcal{L}}$. These are tensors 3, 4, 9, and 24 (indicated by $\parallel$ in Table I). Tensor 4 predicts

TABLE I. List of axial tensors of rank 5 allowed by symmetry in Mn_2Au. The notation introduced in Eq. (19) is used. ∅: The torque perpendicular to the Néel vector is zero. ↗: The torque is nonzero only when the Néel vector is tilted out of the xy plane. ∥: The torque is nonzero when the Néel vector lies in the xy plane. ⊥: The torque is nonzero when the Néel vector points in the z direction. A number in {}-braces specifies the tensor that can be used as a replacement.

Tensor	$\chi^{(5a)}_{ijklm}$	Remark	Tensor	$\chi^{(5a)}_{ijklm}$	Remark
1	⟨13211⟩ − ⟨23122⟩	∅	16	⟨31233⟩ − ⟨32133⟩	∅
2	⟨11213⟩ − ⟨22123⟩	↗	17	⟨13233⟩ − ⟨23133⟩	⊥
3	⟨23212⟩ − ⟨13121⟩	∥	18	⟨12333⟩ − ⟨21333⟩	{17}
4	⟨32221⟩ − ⟨31112⟩	∥	19	⟨22231⟩ − ⟨11132⟩	{6}
5	⟨33213⟩ − ⟨33123⟩	↗	20	⟨11231⟩ − ⟨22132⟩	{2}
6	⟨11123⟩ − ⟨22213⟩	↗	21	⟨12232⟩ − ⟨21131⟩	↗
7	⟨12113⟩ − ⟨21223⟩	{2}	22	⟨12223⟩ − ⟨21113⟩	{21}
8	⟨23221⟩ − ⟨13112⟩	{3}	23	⟨11312⟩ − ⟨22321⟩	{3}
9	⟨21311⟩ − ⟨12322⟩	∥	24	⟨31211⟩ − ⟨32122⟩	∥
10	⟨33231⟩ − ⟨33132⟩	{5}	25	⟨33321⟩ − ⟨33312⟩	∅
11	⟨12131⟩ − ⟨21232⟩	{2}	26	⟨13222⟩ − ⟨23111⟩	{9}
12	⟨31332⟩ − ⟨32331⟩	{5}	27	⟨32212⟩ − ⟨31121⟩	{4}
13	⟨13332⟩ − ⟨23331⟩	↗	28	⟨12311⟩ − ⟨21322⟩	∅
14	⟨31323⟩ − ⟨32313⟩	{5}	29	⟨11321⟩ − ⟨22312⟩	{3}
15	⟨13323⟩ − ⟨23313⟩	{13}	30	⟨31222⟩ − ⟨32111⟩	{24}

torques in the z direction for light polarized linearly in the x direction or in the y direction. Note that the torque from tensor 4 vanishes when the in-plane Néel vector is parallel or perpendicular to the x axis, i.e., when either $\mathcal{L}_x = 0$ or $\mathcal{L}_y = 0$.

Of course, tensor 4 predicts torques also for circularly polarized light. For example, tensor 4 predicts torques for light circularly polarized in the yz plane or in the xz plane. However, the response is even in the light helicity λ. Note that for light circularly polarized in the xy plane the two terms in tensor 4, ⟨32221⟩ and ⟨31112⟩, cancel each other.

Tensor 3 predicts a torque in the y direction for linearly polarized light with $\boldsymbol{\epsilon}$ in the yz plane and a torque in the x direction for linearly polarized light with $\boldsymbol{\epsilon}$ in the zx plane. Tensor 9 predicts a torque in the y direction when the magnetization is along the x direction and when $\boldsymbol{\epsilon}$ lies in the zx plane, and it predicts a torque in the x direction when the magnetization is along the y direction and when $\boldsymbol{\epsilon}$ lies in the yz plane.

While the Néel vector in Mn_2Au lies in the xy plane, there might be AFMs with the same crystal structure as Mn_2Au but with a different magnetic anisotropy, for which $\mathcal{L}_z \neq 0$ might be relevant. Therefore, we discuss the cases with $\mathcal{L}_z \neq 0$ in the following. The case with $\hat{\boldsymbol{\mathcal{L}}} \| \hat{\boldsymbol{e}}_z$ is described by tensor 17 (indicated by ⊥ in the table). This tensor predicts a torque in the x direction when $\boldsymbol{\epsilon}$ lies in the yz plane, and it predicts a torque in the y direction when $\boldsymbol{\epsilon}$ lies in the zx plane.

III. RESULTS

A. Computational details

We employ the full-potential linearized augmented plane-wave program FLEUR [38] in order to determine the electronic structure of Mn_2Au self-consistently within the generalized gradient approximation [39] to density-functional theory. The space group of Mn_2Au is $I4/mmm$. We use the experimental lattice parameters, which are $a = 3.328$ Å and $c = 8.539$ Å for the conventional tetragonal unit cell containing 2 f.u. [40]. In our calculations we use the primitive unit cell, which contains two Mn atoms. We perform calculations with and without SOI in order to test the accuracy of the WISOI. The magnetic moments of the Mn atoms are $3.73\mu_B$.

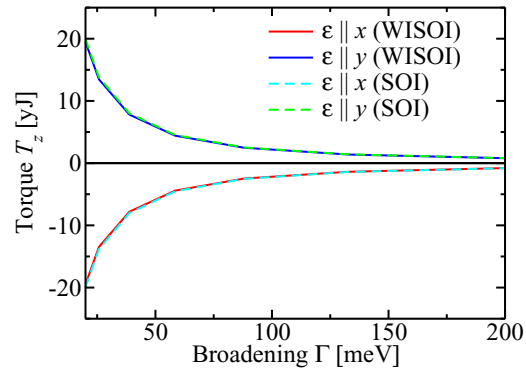

FIG. 1. Laser-induced torque in Mn_2Au vs quasiparticle broadening Γ when the Néel vector points in the 110 direction. Comparison between the results obtained within the WISOI approach (solid lines) and the results obtained based on MLWFs that include SOI (dashed lines). The torque is shown in units of yJ = yoctojoule = 10^{-24} joule.

In order to perform the Brillouin zone integrations in Eq. (2) computationally efficiently based on the Wannier interpolation technique, we constructed 18 MLWFs per transition metal atom from an $8 \times 8 \times 8$ $\boldsymbol{k}$ mesh [27,41] when SOI is included in the calculations. In order to prepare MLWFs for the WISOI approach we constructed 9 MLWFs per transition metal atom and per spin. While these are in total 18 MLWFs per transition metal atom as well, two separate runs of WANNIER90 are performed, one for spin up and one for spin down. The numerical effort needed to obtain two sets of MLWFs without SOI, where each set contains 9 MLWFs per transition metal atom and per spin, is smaller than the numerical effort needed to obtain 18 MLWFs with SOI per transition metal atom because the spin-up and spin-down bands are decoupled in the former case.

B. Laser-induced torques at optical frequencies

In this section we discuss laser-induced torques for the laser intensity $I = 10$ GW/cm^2 when the photon energy is set to 1.55 eV. In Fig. 1 we show the laser-induced torque as a function of Γ when the Néel vector points in the 110 direction. This torque is consistent with tensor 4 in Table I, which describes a laser-induced torque in the z direction that differs in sign for linearly polarized light along the x and y directions. Figure 1 shows both the results obtained within the WISOI approach (solid lines) and the results obtained based on MLWFs that include SOI (dashed lines). The very good agreement between the two approaches proves the validity and accuracy of the WISOI approach. Therefore, all following figures show only the WISOI results. In Fig. 1 we present the torque in units of yoctojoules. The effective staggered magnetic field that produces a torque of 1 yJ is 14.5 mT. Thus, the torques shown in Fig. 1 are of the same order of magnitude

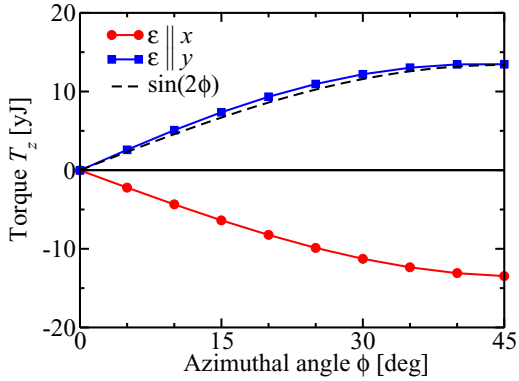

FIG. 2. Laser-induced torque in Mn_2Au vs azimuthal angle ϕ when the polar angle is $\theta = 90^\circ$ and when $\Gamma = 25$ meV.

as the laser-induced torques in the ferromagnets Fe, Co, and FePt, which we studied in Ref. [11].

Tensor 4 predicts a torque in the z direction also for light circularly polarized in the yz or zx plane. Our calculations confirm this prediction. For light circularly polarized in the zx plane we find $T_z < 0$, and its magnitude is half of the magnitude for linearly polarized light with $\boldsymbol{\epsilon} \| \hat{\boldsymbol{e}}_x$. Similarly, for light circularly polarized in the yz plane we find T_z to be half of what it is when $\boldsymbol{\epsilon} \| \hat{\boldsymbol{e}}_y$.

In order to discuss the dependence of the laser-induced torque on the Néel vector we introduce the azimuthal angle ϕ and the polar angle θ such that $\hat{\boldsymbol{\mathcal{L}}} = (\sin\theta\cos\phi, \sin\theta\sin\phi, \cos\theta)^{\mathrm{T}}$. In Fig. 2 we show the laser-induced torque as a function of the azimuthal angle ϕ when $\theta = 90^\circ$ and when the quasiparticle broadening is set to $\Gamma = 25$ meV. Tensor 4 predicts the ϕ dependence $\propto \hat{M}_x\hat{M}_y \propto \sin\phi\cos\phi \propto \sin(2\phi)$, which is illustrated in Fig. 2 by the dashed line and which fits the *ab initio* data very well.

In Fig. 3 we plot the component T_y when the magnetization is along the x direction and when $\boldsymbol{\epsilon} = (\hat{\boldsymbol{e}}_x + \hat{\boldsymbol{e}}_z)/\sqrt{2}$ i.e., $\boldsymbol{\epsilon}\|(101)$. This torque is consistent with tensor 9, which predicts a torque in the y direction when the magnetization is along the x direction and when $\boldsymbol{\epsilon}$ lies in the zx plane.

Next, we discuss the case $\hat{\boldsymbol{\mathcal{L}}} = \hat{\boldsymbol{e}}_z$. In Fig. 4 we show T_y for $\boldsymbol{\epsilon} = (\hat{\boldsymbol{e}}_x + \hat{\boldsymbol{e}}_z)/\sqrt{2}$, i.e., $\boldsymbol{\epsilon}\|(101)$, and T_x for $\boldsymbol{\epsilon} = (\hat{\boldsymbol{e}}_y + \hat{\boldsymbol{e}}_z)/\sqrt{2}$, i.e., $\boldsymbol{\epsilon}\|(011)$. The torques T_x and T_y are equal but opposite in Fig. 4, consistent with tensor 17 in Table I.

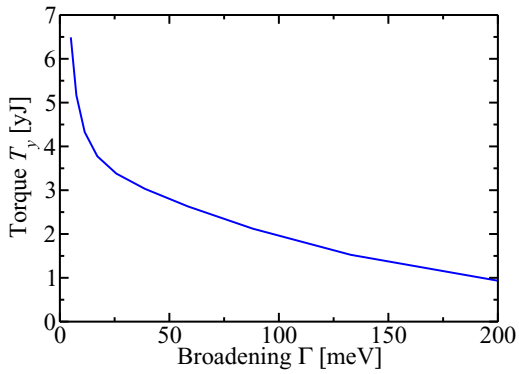

FIG. 3. Laser-induced torque in Mn_2Au vs quasiparticle broadening Γ when the staggered magnetization is along (100), i.e., $\hat{\boldsymbol{\mathcal{L}}} = \hat{\boldsymbol{e}}_x$, and when $\boldsymbol{\epsilon} = (\hat{\boldsymbol{e}}_x + \hat{\boldsymbol{e}}_z)/\sqrt{2}$, i.e., $\boldsymbol{\epsilon}\|(101)$.

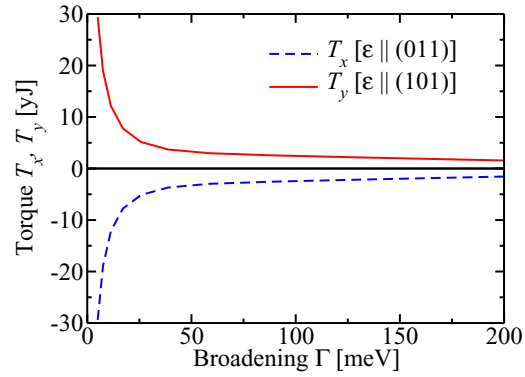

FIG. 4. Laser-induced torque in Mn_2Au vs quasiparticle broadening Γ when the staggered magnetization is along (001), i.e., $\hat{\boldsymbol{\mathcal{L}}} = \hat{\boldsymbol{e}}_z$.

C. Laser-induced torques at THz frequencies

In Fig. 5 we show the laser-induced torque for a THz laser with a frequency of 1 THz for laser intensity $I = 10\,\mathrm{GW/cm^2}$. The intensity $I = 10\,\mathrm{GW/cm^2}$ corresponds to an electric field of the laser light of $E = 2.7\,\mathrm{MV/cm}$. The SOT in Mn_2Au is described by the odd torkance $t^{\mathrm{odd}} = 0.6ea_0$ at $\Gamma = 25$ meV. The corresponding torque at $E = 2.7\,\mathrm{MV/cm}$ is 1370 yJ. This is larger than the maximum laser-induced torque in Fig. 5 by only a factor of 2. At higher broadening $\Gamma = 130$ meV we find a SOT of 230 yJ ($t^{\mathrm{odd}} = 0.1ea_0$) and a laser-induced torque of 12 yJ. The ratio of SOT to the laser-induced torque is thus increased to a factor of 20 by the increase of broadening. At even higher broadening $\Gamma = 200$ meV we find a SOT of 132 yJ ($t^{\mathrm{odd}} = 0.058ea_0$) and a laser-induced torque of 2.6 yJ; that is, the ratio of SOT to the laser-induced torque is further increased to 50.

In the experiment on CuMnAs in Ref. [19] it was shown that THz electric field pulses switch the Néel vector. This switching was attributed to the action of the SOT. We therefore compare the magnitudes of the SOT and of the laser-induced

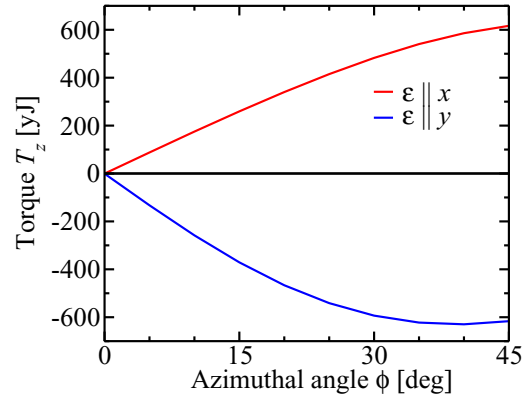

FIG. 5. Laser-induced torque in Mn_2Au vs azimuthal angle ϕ when the polar angle is $\theta = 90^\circ$ and when $\Gamma = 25$ meV.

torque in Mn_2Au in order to judge if the laser-induced torque might contribute as well to the switching by THz pulses. In Ref. [19] the maximum amplitude of the applied THz electric field is $E = 0.11$ MV/cm, which is smaller than $E = 2.7$ MV/cm by a factor 24.5 and which corresponds to an intensity of only 0.017 GW/cm^2. At such a small intensity the ratio of the SOT to the laser-induced torque is roughly 50 in Mn_2Au, such that the laser-induced torque is negligible in Mn_2Au already at $\Gamma = 25$ meV. As discussed in the previous paragraph, the ratio of the SOT to the laser-induced torque will further increase by an order of magnitude when the broadening is increased to $\Gamma = 130$ meV such that the contribution of the laser-induced torques relative to the SOT decreases even further with increasing broadening. Since the laser-induced torque scales quadratically with the electric field of the laser, it becomes more important relative to the SOT at higher fields. However, picosecond THz pulses with intensities as high as $I = 10$ GW/cm^2 are far above the damage threshold of CuMnAs.

While literature values for the damage threshold of Mn_2Au are not available, we assume that picosecond THz pulses of intensities as high as $I = 10$ GW/cm^2 cannot be applied to Mn_2Au without damaging it. In order to apply such high laser intensities without damaging the metallic AFMs much shorter femtosecond pulses are necessary. Therefore, we expect the SOTs from THz laser pulses to be more important than the laser-induced torques. However, when lasers with optical frequencies are used, the SOT oscillates with the frequency of the laser field, which is much higher than the AFM resonance frequencies, and therefore, the SOT cannot excite the AFM. Therefore, when lasers in the optical range are used, the laser-induced torques are important, while the SOT is irrelevant.

IV. SUMMARY

We computed the laser-induced torques in the AFM Mn_2Au based on the Keldysh nonequilibrium approach. We found the laser-induced torques to be of the same order of magnitude as those in the ferromagnets Fe, Co, and FePt. From the phenomenological theory of the IFE in nonmagnets one intuitively expects that laser-induced torques can be generated only by circularly polarized light. In contrast, we found that linearly polarized light is sufficient to stimulate torques in Mn_2Au. We corroborated this finding by a detailed symmetry analysis of the laser-induced torque. Additionally, we discussed the laser-induced torques at THz frequencies. At THz frequencies we compared the laser-induced torque to the SOT and found the SOT to be larger than the laser-induced torque by a factor of 50 at the light intensity used in experiments. In contrast, at optical frequencies only the laser-induced torque induces magnetization dynamics, and the SOT may be neglected. In order to compute response coefficients from Wannier interpolation conveniently for many magnetization directions we developed the WISOI approach. We demonstrated that the WISOI approach reproduces the response coefficients obtained from MLWFs that include SOI with high accuracy.

ACKNOWLEDGMENTS

We acknowledge financial support from Leibniz Collaborative Excellence project OptiSPIN–Optical Control of Nanoscale Spin Textures and funding under SPP 2137 "Skyrmionics" of the Deutsche Forschungsgemeinschaft (DFG, German Research Foundation). We gratefully acknowledge financial support from the European Research Council (ERC) under the European Union's Horizon 2020 research and innovation program (Grant No. 856538, project "3D MAGiC"). The work was also supported by the DFG, TRR 173–268565370 (project A11) and TRR 288–422213477 (project B06). We also gratefully acknowledge the Jülich Supercomputing Centre and RWTH Aachen University for providing computational resources under Project No. jiff40.

APPENDIX: SPIN-ORBIT COUPLING MATRIX ELEMENTS

In this Appendix we describe a procedure that allows us to use MLWFs that are calculated without SOI in order to compute material property tensors including the effect of SOI by adding the effect of SOI during the Wannier interpolation. The advantage of this procedure is that only two sets of MLWFs need to be calculated: one set of MLWFs for the spin-up states and a second set of MLWFs for the spin-down states.

We decompose the Hamiltonian as follows:

$$H = \bar{H} + \mathcal{V}_{\mathrm{SOI}}, \tag{A1}$$

where $\mathcal{V}_{\mathrm{SOI}}$ denotes SOI and $\bar{H}$ is the Hamiltonian without SOI. In order to obtain MLWFs without SOI, $\mathcal{V}_{\mathrm{SOI}}$ is ignored during the generation of MLWFs. We denote the MLWFs without SOI by $|\bar{W}_{\boldsymbol{R}n\sigma}\rangle$, where $\sigma = \uparrow, \downarrow$ labels the spin. The number of spin-up MLWFs is $N_\uparrow$, and the number of spin-down MLWFs is $N_\downarrow$. The total number of MLWFs is $N_{\mathrm{W}} = N_\uparrow + N_\downarrow$. The MLWFs are related to the Bloch functions by the transformation [27]

$$|\bar{W}_{\boldsymbol{R}n\sigma}\rangle = \frac{1}{\mathcal{N}} \sum_{\boldsymbol{k}} e^{-i\boldsymbol{k}\cdot\boldsymbol{R}} \sum_m U^{(\boldsymbol{k})}_{mn\sigma} |\bar{\psi}_{\boldsymbol{k}m\sigma}\rangle, \tag{A2}$$

where $\mathcal{N}$ is the number of $\boldsymbol{k}$ points used for the generation of the MLWFs and where the Bloch states $|\bar{\psi}_{\boldsymbol{k}m\sigma}\rangle$ are the eigenstates of the Hamiltonian $\bar{H}$ without SOI with corresponding eigenvalues $\bar{\mathcal{E}}_{\boldsymbol{k}n\sigma}$, i.e.,

$$\bar{H}|\bar{\psi}_{\boldsymbol{k}n\sigma}\rangle = \bar{\mathcal{E}}_{\boldsymbol{k}n\sigma}|\bar{\psi}_{\boldsymbol{k}n\sigma}\rangle. \tag{A3}$$

The WANNIER90 code [27] determines the transformation $U^{(\boldsymbol{k})}_{mn\sigma}$ such that the resulting Wannier functions are maximally localized.

The Wannier-interpolated Hamiltonian matrix $\bar{\boldsymbol{H}}^{\mathrm{W}}_{\boldsymbol{k}}$ without SOI is given by the Fourier transform [27]

$$\bar{\boldsymbol{H}}^{\mathrm{W}}_{\boldsymbol{k}} = \begin{pmatrix} \bar{\boldsymbol{h}}^{\uparrow\uparrow}_{\boldsymbol{k}} & 0 \\ 0 & \bar{\boldsymbol{h}}^{\downarrow\downarrow}_{\boldsymbol{k}} \end{pmatrix} = \sum_{\boldsymbol{R}} e^{i\boldsymbol{k}\cdot\boldsymbol{R}} \begin{pmatrix} \bar{\boldsymbol{h}}^{\uparrow\uparrow}_{\boldsymbol{R}} & 0 \\ 0 & \bar{\boldsymbol{h}}^{\downarrow\downarrow}_{\boldsymbol{R}} \end{pmatrix}, \tag{A4}$$

where $\bar{\boldsymbol{h}}^{\uparrow\uparrow}_{\boldsymbol{k}}$ and $\bar{\boldsymbol{h}}^{\uparrow\uparrow}_{\boldsymbol{R}}$ are $N_\uparrow \times N_\uparrow$ matrices and $\bar{\boldsymbol{h}}^{\downarrow\downarrow}_{\boldsymbol{k}}$ and $\bar{\boldsymbol{h}}^{\downarrow\downarrow}_{\boldsymbol{R}}$ are $N_\downarrow \times N_\downarrow$ matrices. $\bar{\boldsymbol{H}}^{\mathrm{W}}_{\boldsymbol{k}}$ is a $N_{\mathrm{W}} \times N_{\mathrm{W}}$ matrix. The matrix

elements of $\bar{\boldsymbol{h}}_{\boldsymbol{R}}^{\sigma\sigma}$ are given by [27]

$$\bar{h}^{\sigma\sigma}_{\boldsymbol{R}nm} = \langle \bar{W}_{\boldsymbol{0}n\sigma}|\bar{H}|\bar{W}_{\boldsymbol{R}m\sigma}\rangle = \frac{1}{\mathcal{N}}\sum_{\boldsymbol{k}m'} \bar{\mathcal{E}}_{\boldsymbol{k}m'\sigma} e^{-i\boldsymbol{k}\cdot\boldsymbol{R}} \big(U^{(\boldsymbol{k})}_{m'n\sigma}\big)^* U^{(\boldsymbol{k})}_{m'm\sigma}. \tag{A5}$$

Since SOI is important only close to the nuclei, we may neglect SOI in the interstitial regions between the atoms. We may therefore express SOI as

$$\mathcal{V}_{\mathrm{SOI}} = \sum_{\alpha} \xi_{\alpha}(\boldsymbol{r}-\boldsymbol{r}_{\alpha})\boldsymbol{L}^{\alpha}\cdot\boldsymbol{\sigma}, \tag{A6}$$

where

$$\xi_{\alpha}(\boldsymbol{r}) = \begin{cases} \frac{\mu_{\mathrm{B}}}{2cr}\frac{dV_{\alpha}(r)}{dr} & \text{for } |\boldsymbol{r}| < R_{\alpha}, \\ 0 & \text{for } |\boldsymbol{r}| > R_{\alpha} \end{cases} \tag{A7}$$

is the SOI potential in a sphere around atom α, R_{α} is the atomic radius of atom α, $\boldsymbol{r}_{\alpha}$ is the position of the center of atom α, $\boldsymbol{L}^{\alpha} = (\boldsymbol{r}-\boldsymbol{r}_{\alpha})\times\boldsymbol{p}$ is the angular momentum operator of atom α, and $V_{\alpha}(r)$ is the spherical part of the potential in the sphere around atom α.

In order to add the effect of SOI the following matrix elements need to be evaluated in the basis of Bloch functions:

$$\mathcal{A}^{\sigma\sigma'-}_{\boldsymbol{k}nm} = \sum_{\alpha}\langle\bar{\psi}_{\boldsymbol{k}n\sigma}|\xi_{\alpha}(\boldsymbol{r}-\boldsymbol{r}_{\alpha})L^{\alpha}_{-}|\bar{\psi}_{\boldsymbol{k}m\sigma'}\rangle, \tag{A8}$$

$$\mathcal{A}^{\sigma\sigma'+}_{\boldsymbol{k}nm} = \sum_{\alpha}\langle\bar{\psi}_{\boldsymbol{k}n\sigma}|\xi_{\alpha}(\boldsymbol{r}-\boldsymbol{r}_{\alpha})L^{\alpha}_{+}|\bar{\psi}_{\boldsymbol{k}m\sigma'}\rangle, \tag{A9}$$

and

$$\mathcal{A}^{\sigma\sigma'z}_{\boldsymbol{k}nm} = \sum_{\alpha}\langle\bar{\psi}_{\boldsymbol{k}n\sigma}|\xi_{\alpha}(\boldsymbol{r}-\boldsymbol{r}_{\alpha})L^{\alpha}_{z}|\bar{\psi}_{\boldsymbol{k}m\sigma'}\rangle, \tag{A10}$$

where $L^{\alpha}_{+} = (L^{\alpha}_{x} + iL^{\alpha}_{y})$ and $L^{\alpha}_{-} = (L^{\alpha}_{x} - iL^{\alpha}_{y})$. These matrix elements satisfy the relations

$$\begin{aligned} \mathcal{A}^{\uparrow\uparrow z}_{\boldsymbol{k}mn} &= \big[\mathcal{A}^{\uparrow\uparrow z}_{\boldsymbol{k}nm}\big]^*, \quad \mathcal{A}^{\uparrow\uparrow +}_{\boldsymbol{k}mn} = \big[\mathcal{A}^{\uparrow\uparrow -}_{\boldsymbol{k}nm}\big]^*, \\ \mathcal{A}^{\downarrow\downarrow z}_{\boldsymbol{k}mn} &= \big[\mathcal{A}^{\downarrow\downarrow z}_{\boldsymbol{k}nm}\big]^*, \quad \mathcal{A}^{\downarrow\downarrow +}_{\boldsymbol{k}mn} = \big[\mathcal{A}^{\downarrow\downarrow -}_{\boldsymbol{k}nm}\big]^*, \\ \mathcal{A}^{\downarrow\uparrow z}_{\boldsymbol{k}mn} &= \big[\mathcal{A}^{\uparrow\downarrow z}_{\boldsymbol{k}nm}\big]^*, \quad \mathcal{A}^{\downarrow\uparrow +}_{\boldsymbol{k}mn} = \big[\mathcal{A}^{\uparrow\downarrow -}_{\boldsymbol{k}nm}\big]^*. \end{aligned} \tag{A11}$$

Subsequently, these matrix elements are transformed into the MLWF basis:

$$\begin{aligned} \mathcal{A}^{\sigma\sigma' j}_{\boldsymbol{R}nm} &= \sum_{\alpha}\langle\bar{W}_{\boldsymbol{0}n\sigma}|\xi_{\alpha}(\boldsymbol{r}-\boldsymbol{r}_{\alpha})L^{\alpha}_{j}|\bar{W}_{\boldsymbol{R}m\sigma'}\rangle \\ &= \frac{1}{\mathcal{N}}\sum_{\boldsymbol{k}n'm'} e^{-i\boldsymbol{k}\cdot\boldsymbol{R}}\big[U^{(\boldsymbol{k})}_{n'n\sigma}\big]^* U^{(\boldsymbol{k})}_{m'm\sigma'}\mathcal{A}^{\sigma\sigma' j}_{\boldsymbol{k}n'm'}, \end{aligned} \tag{A12}$$

where $j = -, z, +$.

When the (staggered) magnetization points into the direction $\hat{\boldsymbol{\mathcal{L}}} = (\sin\theta\cos\phi, \sin\theta\sin\phi, \cos\theta)^{\mathrm{T}}$ the spinor of the spin-up electrons is

$$|\uparrow,\theta,\phi\rangle = \begin{pmatrix} e^{-i\phi/2}\cos(\theta/2) \\ e^{i\phi/2}\sin(\theta/2) \end{pmatrix}, \tag{A13}$$

while the spinor of the spin-down electrons is

$$|\downarrow,\theta,\phi\rangle = \begin{pmatrix} -e^{-i\phi/2}\sin(\theta/2) \\ e^{i\phi/2}\cos(\theta/2) \end{pmatrix}. \tag{A14}$$

We define

$$\sigma_{+} = \sigma_{x} + i\sigma_{y}, \quad \sigma_{-} = \sigma_{x} - i\sigma_{y}. \tag{A15}$$

The matrix elements of σ_z are

$$\begin{aligned} \langle\uparrow,\theta,\phi|\sigma_z|\uparrow,\theta,\phi\rangle &= \cos\theta, \\ \langle\downarrow,\theta,\phi|\sigma_z|\downarrow,\theta,\phi\rangle &= -\cos\theta, \\ \langle\uparrow,\theta,\phi|\sigma_z|\downarrow,\theta,\phi\rangle &= -\sin\theta, \\ \langle\downarrow,\theta,\phi|\sigma_z|\uparrow,\theta,\phi\rangle &= -\sin\theta. \end{aligned} \tag{A16}$$

The matrix elements of σ_+ are

$$\begin{aligned} \langle\uparrow,\theta,\phi|\sigma_+|\uparrow,\theta,\phi\rangle &= \sin\theta e^{i\phi}, \\ \langle\downarrow,\theta,\phi|\sigma_+|\downarrow,\theta,\phi\rangle &= -\sin\theta e^{i\phi}, \\ \langle\downarrow,\theta,\phi|\sigma_+|\uparrow,\theta,\phi\rangle &= -2\left[\sin\frac{\theta}{2}\right]^2 e^{i\phi}, \\ \langle\uparrow,\theta,\phi|\sigma_+|\downarrow,\theta,\phi\rangle &= 2\left[\cos\frac{\theta}{2}\right]^2 e^{i\phi}. \end{aligned} \tag{A17}$$

The matrix elements of σ_- are

$$\begin{aligned} \langle\uparrow,\theta,\phi|\sigma_-|\uparrow,\theta,\phi\rangle &= \sin\theta e^{-i\phi}, \\ \langle\downarrow,\theta,\phi|\sigma_-|\downarrow,\theta,\phi\rangle &= -\sin\theta e^{-i\phi}, \\ \langle\downarrow,\theta,\phi|\sigma_-|\uparrow,\theta,\phi\rangle &= 2\left[\cos\frac{\theta}{2}\right]^2 e^{-i\phi}, \\ \langle\uparrow,\theta,\phi|\sigma_-|\downarrow,\theta,\phi\rangle &= -2\left[\sin\frac{\theta}{2}\right]^2 e^{-i\phi}. \end{aligned} \tag{A18}$$

The product $\boldsymbol{L}^{\alpha}\cdot\boldsymbol{\sigma}$ in Eq. (A6) may be rewritten as $\boldsymbol{L}^{\alpha}\cdot\boldsymbol{\sigma} = L^{\alpha}_{z}\sigma_{z} + [L^{\alpha}_{+}\sigma_{-} + L^{\alpha}_{-}\sigma_{+}]/2$. Therefore, we need to multiply the matrix elements in Eq. (A12) by the angular factors in Eqs. (A16), (A17), and (A18) in order to obtain the matrix elements of the SOI Hamiltonian (A6) in the basis set of the MLWFs without SOI. The resulting matrix elements are given in Eqs. (6), (7), (8), and (9) in the main text.

[1] C.-H. Lambert, S. Mangin, B. S. D. C. S. Varaprasad, Y. K. Takahashi, M. Hehn, M. Cinchetti, G. Malinowski, K. Hono, Y. Fainman, M. Aeschlimann, and E. E. Fullerton, All-optical control of ferromagnetic thin films and nanostructures, Science **345**, 1337 (2014).

[2] R. John, M. Berritta, D. Hinzke, C. Müller, T. Santos, H. Ulrichs, P. Nieves, J. Walowski, R. Mondal, O. Chubykalo-Fesenko, J. McCord, P. M. Oppeneer, U. Nowak, and M. Münzenberg, Magnetisation switching of FePt nanoparticle recording medium by femtosecond laser pulses, Sci. Rep. **7**, 4114 (2017).

[3] A. V. Kimel, A. Kirilyuk, P. A. Usachev, R. V. Pisarev, A. M. Balbashov, and T. Rasing, Ultrafast non-thermal control of magnetization by instantaneous photomagnetic pulses, Nature (London) **435**, 655 (2005).

[4] P. Nemec, E. Rozkotova, N. Tesarova, F. Trojanek, E. De Ranieri, K. Olejnik, J. Zemen, V. Novak, M. Cukr, P. Maly, and T. Jungwirth, Experimental observation of the optical spin transfer torque, Nat. Phys. **8**, 411 (2012).

[5] T. J. Huisman, R. V. Mikhaylovskiy, J. D. Costa, F. Freimuth, E. Paz, J. Ventura, P. P. Freitas, S. Blügel, Y. Mokrousov, T. Rasing, and A. V. Kimel, Femtosecond control of electric currents in metallic ferromagnetic heterostructures, Nat. Nanotechnol. **11**, 455 (2016).

[6] M. van Kampen, C. Jozsa, J. T. Kohlhepp, P. LeClair, L. Lagae, W. J. M. de Jonge, and B. Koopmans, All-Optical Probe of Coherent Spin Waves, Phys. Rev. Lett. **88**, 227201 (2002).

[7] A. J. Schellekens, K. C. Kuiper, R. R. J. C. de Wit, and B. Koopmans, Ultrafast spin-transfer torque driven by femtosecond pulsed-laser excitation, Nat. Commun. **5**, 4333 (2014).

[8] G.-M. Choi, C.-H. Moon, B.-C. Min, K.-J. Lee, and D. G. Cahill, Thermal spin-transfer torque driven by the spin-dependent Seebeck effect in metallic spin-valves, Nat. Phys. **11**, 576 (2015).

[9] A. Capua, C. Rettner, S.-H. Yang, T. Phung, and S. S. P. Parkin, Ensemble-averaged Rabi oscillations in a ferromagnetic CoFeB film, Nat. Commun. **8**, 16004 (2017).

[10] G.-M. Choi, A. Schleife, and D. G. Cahill, Optical-helicity-driven magnetization dynamics in metallic ferromagnets, Nat. Commun. **8**, 15085 (2017).

[11] F. Freimuth, S. Blügel, and Y. Mokrousov, Laser-induced torques in metallic ferromagnets, Phys. Rev. B **94**, 144432 (2016).

[12] P. Baláž, K. Carva, U. Ritzmann, P. Maldonado, and P. M. Oppeneer, Domain wall dynamics due to femtosecond laser-induced superdiffusive spin transport, Phys. Rev. B **101**, 174418 (2020).

[13] U. Ritzmann, P. Baláž, P. Maldonado, K. Carva, and P. M. Oppeneer, High-frequency magnon excitation due to femtosecond spin-transfer torques, Phys. Rev. B **101**, 174427 (2020).

[14] A. Qaiumzadeh and M. Titov, Theory of light-induced effective magnetic field in Rashba ferromagnets, Phys. Rev. B **94**, 014425 (2016).

[15] M. Berritta, R. Mondal, K. Carva, and P. M. Oppeneer, *Ab Initio* Theory of Coherent Laser-Induced Magnetization in Metals, Phys. Rev. Lett. **117**, 137203 (2016).

[16] V. Baltz, A. Manchon, M. Tsoi, T. Moriyama, T. Ono, and Y. Tserkovnyak, Antiferromagnetic spintronics, Rev. Mod. Phys. **90**, 015005 (2018).

[17] A. Manchon, J. Železný, I. M. Miron, T. Jungwirth, J. Sinova, A. Thiaville, K. Garello, and P. Gambardella, Current-induced spin-orbit torques in ferromagnetic and antiferromagnetic systems, Rev. Mod. Phys. **91**, 035004 (2019).

[18] E. V. Gomonay and V. M. Loktev, Spintronics of antiferromagnetic systems (review article), Low Temp. Phys. **40**, 17 (2014).

[19] K. Olejník, T. Seifert, Z. Kašpar, V. Novák, P. Wadley, R. P. Campion, M. Baumgartner, P. Gambardella, P. Němec, J. Wunderlich, J. Sinova, P. Kužel, M. Müller, T. Kampfrath, and T. Jungwirth, Terahertz electrical writing speed in an antiferromagnetic memory, Sci. Adv. **4**, eaar3566 (2018).

[20] J. Železný, H. Gao, K. Výborný, J. Zemen, J. Mašek, A. Manchon, J. Wunderlich, J. Sinova, and T. Jungwirth, Relativistic Néel-Order Fields Induced by Electrical Current in Antiferromagnets, Phys. Rev. Lett. **113**, 157201 (2014).

[21] J. Železný, H. Gao, A. Manchon, F. Freimuth, Y. Mokrousov, J. Zemen, J. Mašek, J. Sinova, and T. Jungwirth, Spin-orbit torques in locally and globally noncentrosymmetric crystals: Antiferromagnets and ferromagnets, Phys. Rev. B **95**, 014403 (2017).

[22] L. Salemi, M. Berritta, A. K. Nandy, and P. M. Oppeneer, Orbitally dominated Rashba-Edelstein effect in noncentrosymmetric antiferromagnets, Nat. Commun. **10**, 5381 (2019).

[23] S. Y. Bodnar, L. Šmejkal, I. Turek, T. Jungwirth, O. Gomonay, J. Sinova, A. A. Sapozhnik, H. J. Elmers, M. Kläui, and M. Jourdan, Writing and reading antiferromagnetic Mn_2Au by Néel spin-orbit torques and large anisotropic magnetoresistance, Nat. Commun. **9**, 348 (2018).

[24] M. Meinert, D. Graulich, and T. Matalla-Wagner, Electrical Switching of Antiferromagnetic Mn_2Au and the Role of Thermal Activation, Phys. Rev. Appl. **9**, 064040 (2018).

[25] X. F. Zhou, J. Zhang, F. Li, X. Z. Chen, G. Y. Shi, Y. Z. Tan, Y. D. Gu, M. S. Saleem, H. Q. Wu, F. Pan, and C. Song, Strong Orientation-Dependent Spin-Orbit Torque in Thin Films of the Antiferromagnet Mn_2Au, Phys. Rev. Appl. **9**, 054028 (2018).

[26] S. Y. Bodnar, M. Filianina, S. P. Bommanaboyena, T. Forrest, F. Maccherozzi, A. A. Sapozhnik, Y. Skourski, M. Kläui, and M. Jourdan, Imaging of current induced Néel vector switching in antiferromagnetic Mn_2Au, Phys. Rev. B **99**, 140409(R) (2019).

[27] G. Pizzi *et al.*, Wannier90 as a community code: New features and applications, J. Phys.: Condens. Matter **32**, 165902 (2020).

[28] M. Battiato, G. Barbalinardo, K. Carva, and P. M. Oppeneer, Beyond linear response theory for intensive light-matter interactions: Order formalism and ultrafast transient dynamics, Phys. Rev. B **85**, 045117 (2012).

[29] F. Freimuth, S. Blügel, and Y. Mokrousov, Charge and spin photocurrents in the Rashba model, Phys. Rev. B **103**, 075428 (2021).

[30] W. Kraut and R. von Baltz, Anomalous bulk photovoltaic effect in ferroelectrics: A quadratic response theory, Phys. Rev. B **19**, 1548 (1979).

[31] R. von Baltz and W. Kraut, Theory of the bulk photovoltaic effect in pure crystals, Phys. Rev. B **23**, 5590 (1981).

[32] Y. Zhang, H. Ishizuka, J. van den Brink, C. Felser, B. Yan, and N. Nagaosa, Photogalvanic effect in Weyl semimetals from first principles, Phys. Rev. B **97**, 241118(R) (2018).

[33] D. Go, F. Freimuth, J.-P. Hanke, F. Xue, O. Gomonay, K.-J. Lee, S. Blügel, P. M. Haney, H.-W. Lee, and Y. Mokrousov, Theory of current-induced angular momentum transfer dynamics in spin-orbit coupled systems, Phys. Rev. Research **2**, 033401 (2020).

[34] S. Ding, A. Ross, D. Go, L. Baldrati, Z. Ren, F. Freimuth, S. Becker, F. Kammerbauer, J. Yang, G. Jakob, Y. Mokrousov, and M. Kläui, Harnessing Orbital-to-Spin Conversion of Interfacial Orbital Currents for Efficient Spin-Orbit Torques, Phys. Rev. Lett. **125**, 177201 (2020).

[35] Y. Tazaki, Y. Kageyama, H. Hayashi, T. Harumoto, T. Gao, J. Shi, and K. Ando, Current-induced torque originating from orbital current, arXiv:2004.09165.

[36] J. Kim, D. Go, H. Tsai, D. Jo, K. Kondou, H.-W. Lee, and Y. C. Otani, Nontrivial torque generation by orbital angular momentum injection in ferromagnetic-metal/Cu/Al_2O_3 trilayers, Phys. Rev. B **103**, L020407 (2021).

[37] A. Johansson, B. Göbel, J. Henk, M. Bibes, and I. Mertig, Spin and orbital Edelstein effects in a two-dimensional electron gas: Theory and application to $SrTiO_3$ interfaces, Phys. Rev. Research **3**, 013275 (2021).

[38] FLEUR, http://www.flapw.de.

[39] J. P. Perdew, K. Burke, and M. Ernzerhof, Generalized Gradient Approximation Made Simple, Phys. Rev. Lett. **77**, 3865 (1996).

[40] P. Wells and J. H. Smith, The structure of Mn_2Au and Mn_3Au, Acta Crystallogr., Sect. A **26**, 379 (1970).

[41] F. Freimuth, Y. Mokrousov, D. Wortmann, S. Heinze, and S. Blügel, Maximally localized Wannier functions within the FLAPW formalism, Phys. Rev. B **78**, 035120 (2008).